Analysis of heat and mass transfer by CFD for performance enhancement in direct contact membrane distillation

Yu, Hui; Yang, Xing; Wang, Rong; Fane, Anthony Gordon

2012

Yu, H., Yang, X., Wang, R., & Fane A. G. (2012). Analysis of heat and mass transfer by CFD for performance enhancement in direct contact membrane distillation. Journal of Membrane Science, 405-406, 38-47.

https://hdl.handle.net/10356/95762

https://doi.org/10.1016/j.memsci.2012.02.035

Analysis of heat and mass transfer by CFD for performance enhancement in direct contact membrane distillation

Hui Yu[1,2,3], Xing Yang[1,2], Rong Wang*[,1,2], Anthony G. Fane[1,2]

1. Singapore Membrane Technology Centre, Nanyang Technological University, Singapore 639798
2. School of Civil and Environmental Engineering, Nanyang Technological University, Singapore 639798
3. School of Chemical Engineering, Sichuan University, China 610065

*Corresponding author at: School of Civil and Environmental Engineering, Nanyang Technological University, 639798 Singapore, Singapore. Tel.: +65 6790 5327; fax: +65 6791 0676.
E-mail address: rwang@ntu.edu.sg (R. Wang).

Abstract

A comprehensive analysis on the dominant effects for heat and mass transfer in the direct contact membrane distillation (DCMD) process has been performed with the aid of computational fluid dynamics (CFD) simulations for hollow fiber modules without and with annular baffles attached to the shell wall. Potential enhancement strategies under different circumstances have been investigated.

Numerical simulations were carried out to investigate the effect of the MD intrinsic mass-transfer coefficient of the membrane (*C*) on the performance enhancement for both non-baffled and baffled modules. It was found that the temperature polarization coefficient (*TPC)* decreases significantly with increasing *C* value regardless of the existence of baffles, signifying a loss of overall driving force. However, the higher C compensated for this and the mass flux showed an increasing trend. A membrane with a lower *C* value was found to be less vulnerable to the TP effect. In this case, the introduction of turbulence aids such as baffles did not show substantial effect to improve system performance. In contrast, introducing baffles into the module can greatly enhance the mass flux and the *TPC* for a membrane with a high *C* value, where the main heat-transfer resistance is determined by the fluid side boundary layers.

The effect of operating temperature on heat and mass transfer in the MD process was also studied with a membrane of a lower *C* value (2.0×10^{-7} $kg\cdot m^{-2}\cdot s^{-1}\cdot Pa^{-1}$). Although the *TPC* generally decreased with increasing operating temperatures, the mass flux N_m increased significantly when operating temperature increased. A baffled module showed a more significant improvement than a non-baffle module at a higher temperature. Moreover, it was confirmed that higher operating temperatures are preferable for a substantial improvement in the heat/mass transfer as well as MD thermal efficiency, even with a relatively small transmembrane temperature difference of 10K.

Key words: membrane distillation, computational fluid dynamics, heat-transfer resistance, single fiber module, process enhancement

1. Introduction

Membrane distillation (MD) is an integrated separation process that involves heat and mass transfer. It produces high-quality pure water by utilizing a hydrophobic microporous membrane to separate hot feed and cold permeate, and the transmembrane temperature gradient serves as the driving force for water transfer. In spite of many potential benefits offered by the MD process, such as theoretically 100% rejection for non-volatile impurities, low operating temperatures, no applied hydraulic pressure requirement and reasonably low capital costs, the mass flux of the MD process tends to be rather low compared with other membrane processes such as reverse osmosis (RO) [1]. Severe temperature-polarization (TP), which is attributed to poor fluid dynamics, is believed to be one of the main causes responsible for low water flux, as it leads to a lower actual transmembrane temperature difference. For direct contact membrane distillation (DCMD) where hot and cold fluids are in contact with the membrane, low thermal efficiency can occur due to the conductive heat loss through the membrane matrix and this may have hindered MD commercialization [2]. Therefore, there are two important challenges for MD practical applications, namely the availability of highly permeable membranes and suitable modules with improved hydrodynamics for the MD process.

Surging interest in MD membrane development has been seen in laboratory and industry recently, though there exist only a few highly-permeable membranes [3, 4]. On the other hand, much effort has been devoted to the MD process in order to mitigate the TP effect and further increase permeation flux [5-10]. These studies have examined the permeation flux and flux decay in terms of operating conditions, long term performance, membrane properties, module design and thermal energy consumption, etc [11-13]. It is well-recognized that the feed and permeate temperatures, the vapor pressure difference and the feed and permeate flow velocities play important roles in MD performance [14]. For example, a higher operating temperature and higher flow velocity will result in a higher mass flux. Also, enhanced performance and reduced TP effect could be achieved by other process enhancement approaches such as the introduction of turbulence promoters (e.g.,

channeled design, external baffles and spacers), novel module configuration and optimized fiber geometries, etc [5-9, 15, 16].

However, some of these approaches may result in undesirable effects in industrial applications, such as a higher hydraulic pressure loss due to a higher feed flow velocity, or a greater conductive heat loss caused by a lower permeate temperature [17], etc. Thus, it is essential to fully understand the significance of each parameter and develop methods to predict experimental results and optimize the operating conditions. To achieve this goal, in-situ qualitative predictions using numerical modeling tools have been widely adopted by both laboratory and industrial researchers.

Semi-empirical equations have been used for process modeling and prediction, especially in MD applications [1]. This has proved to be helpful in analyzing the heat-transfer process and calculating the local heat-transfer coefficients and membrane surface temperatures and hence determining the temperature-polarization coefficient [1, 13, 18-20]. Unfortunately, these empirical equations were developed based on non-porous and rigid shell and tube heat exchangers that are not coupled with mass transfer and phase changes [14]. Therefore, the accuracy and applicability of these equations in MD modeling can be questioned. Recently, computational fluid dynamics (CFD) modeling has been adopted and has proved to be a valuable tool in analyzing fluid dynamic behavior in membrane modules [17, 21]. With the benefits of visualizing the flow field (including velocity, pressure, temperature and concentration profiles) at any location in a defined flow channel, CFD modeling can be used to analyze key process design and operating parameters, determine the controlling step in mass- and heat-transfer processes and provide guidance for scale-up. However, to date there is very limited CFD modeling of hollow fiber MD modules in the literature.

Due to the complication of coupled transfer mechanism across bulk fluids and membrane, most prior CFD modeling work on membrane separation processes adopted simplified methods [21]. For example, in numerical simulations of mass transfer processes the commonly used simplified CFD models considered only one fluid and treat the mass flux

as a boundary condition [22, 23]. For simulation of a combined heat and mass transfer process, Zhang et al [24, 25] suggested treating the mass and heat transferred among the membrane and two fluids as a conjugate problem, but ignored phase changes in a membrane-based ventilator system. In MD modeling, Hwang et al [26] incorporated the feed, permeate and membrane into their simulation to obtain velocity and temperature fields. However, the transmembrane mass transport and the latent heat induced by evaporation were ignored. A recent review on the development of CFD modeling stated that most MD researchers tended to ignore the permeate flow and focus on the bulk feed flow and/or simplified transmembrane transfer models [21].

In our recent work [17], a CFD study with an improved heat-transfer model for a single hollow fiber module has been reported, which couples the latent heat into the energy conservation equation and combines this with the Navies-Stokes equations to address the transport between the fluids (feed and permeate) and the membrane [17]. In the present study, this model is further verified by comparing simulation results with experimental data under different operating temperatures. (1) As an extension, a thorough analysis of the heat and mass transfer controlling steps is conducted based on this model to reveal the impacts of key parameters that could contribute to an enhanced direct contact membrane distillation (DCMD) system. Various performance metrics, including the TP coefficient, mass flux and thermal efficiency, are examined as a function of membrane properties (C values) and characteristic membrane temperatures. (2) Further, a MD module with annular baffles attached to the shell wall has been proposed and is modeled to explore the effect of turbulence promoters on enhancing the MD performance. Potential process enhancement strategies under different circumstances are discussed.

2. Theory

2.1 Geometric structure, governing transport equations and boundary conditions in CFD simulation

A non-baffled single hollow fiber module with a length of 0.25 m was chosen as the reference case to be studied both experimentally and numerically. This reference module was then adapted to a novel configuration, which possesses a cylindrical housing with annular baffles attached to the shell wall. Fig. 1 shows the schematic of a 2D axially-symmetric single hollow fiber module with annular baffles, in which R_{mi} and R_{mo} are the inner and outer radii of the fiber, Δx and Δr are the dimensions of the annular baffle in x and r directions, respectively, and Lx is the interval between two baffles. For this study, Δx, Δr and Lx were chosen to be 0.2, 2 and 10 mm, respectively. The feed and permeate fluids flow in a counter-current mode on the shell and lumen sides, respectively.

As mentioned in our previous study [17], in a single fiber module the MD mass flux has a negligible contribution to either the feed or permeate bulk flows when compared to the operating feed flow rate. Thus, in the current work we continue to use and further verify this established heat-transfer model, which combines the latent heat incurred by evaporation/condensation into the heat-transfer process but ignores the influence of the mass flow to the conservation equations in the DCMD process. The governing transport equations and boundary conditions in the CFD simulation have been provided previously [17]. For easy reference, the overall governing transport equations are summarized as follows:

The continuity equation:

$$\nabla \cdot (\rho \vec{v}) = 0 \tag{1}$$

The momentum transport equation:

$$\nabla \cdot (\rho \vec{v} \vec{v}) = -\nabla p + \nabla \cdot (\bar{\bar{\tau}}) + \rho \vec{g} \tag{2}$$

where $\bar{\bar{\tau}}$ is expressed as:

$$\bar{\bar{\tau}} = \mu \left[\left(\nabla \vec{v} + \nabla \vec{v}^T \right) - \frac{2}{3} \nabla \cdot \vec{v} I \right] \tag{3}$$

The energy conservation equation:

$$\nabla \cdot (\vec{v} \rho c_p T) = \nabla \cdot (k \nabla T) + S_h \tag{4}$$

where

$$S_h = \begin{cases} \dfrac{q_{MD}}{\delta r} \cdot \dfrac{R_{mo}}{R_{mi}} & \text{for } r = R_{mi} \\ -\dfrac{q_{MD}}{\delta r} & \text{for } r = R_{mo} \\ 0 & \text{otherwise} \end{cases} \tag{5}$$

And S_h represents the heat flux due to the vapor flow.

Other boundary conditions are applied:

- Entrance of feed and permeate: u_{fi}=0.06 m·s^{-1} (Re_f=836 for the original module), u_{pi}=0.417 m·s^{-1} (Re_p= 460 for the original module), T_{fi} = 327.2 to 337.2 K, T_{pi} = 294.0 to 314 K (note: these are typical experimental values).
- Outlet of feed and permeate: outlet pressure is 0.0 Pa (gauge pressure)
- Membrane wall: no-slip condition, conjugate heat conduction:

$$q_f\big|_{r=R_{mo}} = q_m\big|_{r=R_{mo}},\ q_m\big|_{r=Rmi} = q_p\big|_{r=R_{mi}}$$

$$T_f\big|_{r=R_{mo}} = T_m\big|_{r=R_{mo}},\ T_f\big|_{r=R_{mi}} = T_m\big|_{r=R_{mi}} \tag{6}$$

Based on the above operating conditions, laminar model was applied to the conservation equations for original modules; while in a modified configuration, a realizable *k*-*ε* model [27] with enhanced wall treatment is employed to simulate the turbulence induced by the introduction of baffles.

2.2 Computational domain and algorithm

By assuming the single-fiber modules have a cylindrical structure, a series of 2D axial-symmetric single-fiber domains were built. The quad mesh was adopted for grid generation in this model. To optimize the grid structure, in the radial direction a grid scale of 5×10^{-6} m was chosen for the bulk permeate and membrane, and progressively increasing scales from 5×10^{-6} to 2×10^{-4} m were set for the bulk feed (shell-side); while in the axial direction a universal grid scale of 1×10^{-4}m was employed. The details of the grid scale can be found in an previous work [17]. The effect of the hollow fiber membrane surface roughness on the wall boundary conditions was ignored as it has a magnitude of 10^{-8} m, which is far smaller than the grid scale. The simulations were carried out using the software Fluent 6.3, with SIMPLE (Semi-Implicit Method for Pressure Linked Equations) algorithm for pressure-velocity coupling and QUICK (Quadratic Upstream Interpolation for Convective Kinetics) algorithm for discretization of the conservation equations. The computational accuracy of 10^{-5} was chosen for convergence.

2.3 Resistance analysis of MD heat transfer process

2.3.1 Overall heat-transfer coefficient and heat-transfer coefficient across the membrane

In general, the heat-transfer mechanism in MD involves three steps in series: firstly, heat is transferred from the bulk liquid feed to the hot membrane surface, water molecules evaporate at the surface (at the mouth of the pores); secondly, water vapor carries the heat through the membrane matrix from the hot surface to the cold side, accompanied by latent heat generation and conductive heat loss; finally, the heat is released at the cold membrane surface by condensation and then reaches the bulk permeate [2, 11]. A schematic showing this heat-transfer process is given in Fig. 2, in which h_f and h_p are the heat-transfer

coefficients for the feed and permeate, respectively; h_{MD} and h_{HL} are defined as equivalent heat-transfer coefficients for the heat transfer associated with evaporation and conduction, respectively; the overall heat-transfer rate across the membrane Q is written as:

$$Q = Q_f = Q_p = Q_{MD} + Q_{HL} \tag{7}$$

where Q_f and Q_p represent the heat flowing across the liquid film boundary layers; Q_{MD} is the latent heat incurred from evaporation/condensation of vapor across the membrane and Q_{HL} is the conductive heat loss; T_f and T_p are the bulk temperatures of feed and permeate, respectively, which is defined as:

$$T_b = \frac{\int_S \rho u T \mathrm{d}S}{\int_S \rho u \mathrm{d}S} \tag{8}$$

where ρ and S are density, and cross-sectional area of feed-side or permeate-side, respectively and u is the velocity which normalizes to S. The overall heat-transfer coefficient, K_{mo}, for a hollow fiber module can be expressed as [28]:

$$\frac{1}{K_{mo}} = \frac{1}{h_f} + \frac{1}{h_m} + \frac{1}{h_p} \cdot \frac{R_{mo}}{R_{mi}} \tag{9}$$

where

$$h_m = h_{MD} + h_{HL} \cdot \frac{R_{lm}}{R_{mo}} \tag{10}$$

R_{mi}, R_{mo}, and R_{lm} are the inner, outer and log mean radii of the hollow fiber, respectively; the reciprocals of heat transfer coefficients $1/h$ represent the corresponding local resistances. h_m is the equivalent heat-transfer coefficient of the membrane, where the heat flux across the membrane q_m can be expressed as:

$$q_m = h_m(T_{fm} - T_{pm}) \tag{11}$$

2.3.2 Heat-transfer coefficient of the bulk fluids (feed/permeate)

In an MD system the heat transfer across the liquid films (feed side q_f or permeate side q_p) can be expressed as:

$$q_f = h_f \Delta T_f = h_f (T_f - T_{fm}),\ q_p = h_p \Delta T_p = h_p (T_{pm} - T_p) \tag{12}$$

where h_f and h_p can be calculated using Eq.(12) based on the temperature field obtained from CFD simulations.

2.3.3 Equivalent heat-transfer coefficients due to evaporation and conduction

As the mass and heat transfer are closely related in MD, the latent heat flux q_{MD} is described as:

$$q_{MD} = N_m \cdot \Delta H_{T_{fm}} \tag{13}$$

where $\Delta H_{T_{fm}}$ is the latent heat of evaporation occurring at the membrane surface on the feed side (T_{fm}). N_m is the transmembrane mass flux, kg·m^{-2}·s^{-1}, defined as [11]:

$$N_m = C\,(P_{fm} - P_{pm}) \tag{14}$$

or

$$N_m = C \frac{\mathrm{d}P}{\mathrm{d}T}\Big|_{T=T_m} (T_{fm} - T_{pm}) \tag{15}$$

where the gradient dP/dT is the differential form deduced from the Antoine equation, T_m is the membrane temperature which can be estimated by $(T_f + T_p)/2$. The parameter C is the intrinsic mass-transfer coefficient of the membrane, P_{fm} and P_{pm} are the saturated vapor pressures obtained from Antoine equation [29] at the membrane wall temperatures T_{fm} and T_{pm}, respectively. To obtain the C value for the heat-transfer simulation in MD, various approaches such as the combined Knudsen diffusion, molecular diffusion and Poiseuille

flow transition model [30], Knudsen diffusion model [13, 31] and Monte Carlo simulation method [32] have been reported. Although *C* is dependent on the membrane temperature, it can be taken as a constant with fixed membrane properties under certain operating conditions [33]. Therefore, this study has adopted a similar simplified model and assumes a constant *C*, equal to 2.0×10^{-7} $kg\cdot m^{-2}\cdot s^{-1}\cdot Pa^{-1}$calculated from a series of single-fiber module tests reported previously [9].

The combination of Eqs. (13) and (15) **Error! Reference source not found.**yields the following:

$$q_{MD} = C\frac{\mathrm{d}P}{\mathrm{d}T}\Big|_{T=T_m} \Delta H_{T_m} (T_{fm} - T_{pm}) \tag{16}$$

As defined previously, h_{MD} is the equivalent heat-transfer coefficient for evaporation, so Eq. (16) can be simplified based on Newton's law of cooling [34]:

$$q_{MD} = h_{MD} \cdot (T_{fm} - T_{pm}) \tag{17}$$

Then h_{MD} is expressed as:

$$h_{MD} = C\frac{\mathrm{d}P}{\mathrm{d}T}\Big|_{T=T_m} \Delta H_{T_m} \tag{18}$$

The conductive heat flux q_{HL} through the membrane matrix can be written as:

$$q_{HL} = \frac{k_m}{b} \cdot (T_{fm} - T_{pm}) \tag{19}$$

where k_m and b are the thermal conductivity and thickness of the membrane, respectively. Hence, the equivalent heat-transfer coefficient for conduction is defined as $h_{HL} = \frac{k_m}{b}$, which is a constant for fixed membrane properties.

2.4 Thermal efficiency and characteristic temperature

As mentioned previously, the total heat flux transferred through the membrane is split into two parts: the latent heat of evaporation, which is seen as the effective portion that generates a certain amount of vapor; and the conduction across the membrane matrix, which is considered as heat loss. Hence, MD thermal efficiency η_h is defined as the fraction of the evaporation heat:

$$\eta_h = \frac{Q_{MD}}{Q_{MD}+Q_{HL}} = \frac{h_{MD}\cdot A_{mo}\cdot (T_{fm}-T_{pm})}{\left(h_{MD}+h_{HL}\cdot \frac{R_{lm}}{R_{mo}}\right)\cdot A_{mo}\cdot (T_{fm}-T_{pm})} = \frac{h_{MD}}{h_{MD}+h_{HL}\cdot \frac{R_{lm}}{R_{mo}}} \quad (20)$$

In order to maximize the thermal efficiency η_h, the conductive heat loss should be minimized. To provide a benchmark, we take the value 0.5 as a characteristic efficiency $\eta_{h0.5}$ when the effective heat usage and conductive heat loss are equivalent, and a characteristic membrane temperature T_c is defined and obtained via following equation:

$$f(T_c) = C\frac{\mathrm{d}P}{\mathrm{d}T}\Big|_{T=T_c}\Delta H_{T_c} - \frac{k_m}{b}\frac{R_{lm}}{R_{mo}} = 0 \quad (21)$$

According to our previous study [17], η_h increases with increasing membrane temperature. Thus, to operate a more energy-friendly MD system with η_h greater than 0.5, the membrane temperature should be higher than the characteristic membrane temperature T_c.

The temperature-polarization coefficient (*TPC*) is expressed as [2]:

$$TPC = \frac{T_{fm}-T_{pm}}{T_f - T_p} \quad (22)$$

3. Experimental

This section describes measurements and experiments used to validate the CFD simulation model.

3.1 Materials

In the present study, a hydrophobic polyvinylidene fluoride (PVDF) membrane was characterized experimentally. The properties of the PVDF hollow fiber membrane and testing fluids were presented in our previous work [17].

3.2 DCMD experiment

The DCMD experimental setup for the single fiber module tests is similar to that in the previous work [9]. Both the feed and permeate solutions were cycled through the hollow fiber module in countercurrent mode. On the shell side, the feed solution (synthetic seawater: 3.5 wt% sodium chloride (NaCl) with conductivity around 60 ms·cm^{-1}) was heated (T_{fi} = 327.2 to 337.2 K) and circulated by a peristaltic pump (u_{fi}= 0.06 m·s^{-1}). On the lumen side, the permeate (pure water, with conductivity around 0.5 μs·cm^{-1}) was cooled (T_{pi} = 294.0 to 314.0 K by a cooling circulator and cycled by another peristaltic pump (u_{pi}= 0.417 m·s^{-1}). The distillate was collected in an overflow tank sitting on a balance (±0.1 g) and temperatures monitored by thermal sensors PT100 (±0.05K).

Single-fiber modules with effective fiber length of 0.25 m and membrane area A=0.0011 m^2 were made to investigate the effect of operating temperature. These lab-scale MD modules were fabricated by potting the PVDF hollow fiber membranes into Teflon housings.

4. Results and discussion

4.1 Comparison between experimental data and simulation results

For the current heat-transfer model presented in Section 2.1, our previous CFD work has

verified it via the experimental results of length and temperature variation tests for single fiber modules [17]. To further verify its applicability in our current study, a series of temperature variation tests have been conducted for an original module. The simulated average bulk temperatures from CFD were compared with the experimental results, which are listed in Table. 1. The T_{fo}, and T_{po} are bulk temperatures at the exits of the feed side and the permeate side, respectively. It can be seen that the simulation data agrees very well with the experimental values. The relative errors are within ±5%, which confirmed the reliability of the newly-developed numerical method.

4.2 Dominant resistance in heat-transfer process

Fig. 3 shows the local and overall heat-transfer coefficients for various types of membranes with different C values (ranging from 2.0×10^{-7} to 1.0×10^{-6} $kg\cdot m^{-2}\cdot s^{-1}\cdot Pa^{-1}$) as functions of the dimensionless fiber length x/L. For one specific membrane, e.g., C=2.0×10^{-7} $kg\cdot m^{-2}\cdot s^{-1}\cdot Pa^{-1}$, its feed-side heat-transfer coefficient h_f curve presents an initial decreasing trend due to the entrance effect and then gradually reaches an asymptotic value along the x direction; the distribution of permeate-side heat-transfer coefficient h_p shows the same trend along the $-x$ direction (countercurrent flow pattern). It is noticed that both the membrane and overall heat-transfer coefficients (h_m and K_{mo}) are of the same magnitude, but both are lower than h_f & h_p, and show negligible change along x direction.

In Fig. 3, for different membranes operated under the same hydrodynamic conditions (fixed h_f and h_p), both h_m and K_{mo} increase significantly with increasing C values. For example, a membrane with a low C value of 2.0×10^{-7} $kg\cdot m^{-2}\cdot s^{-1}\cdot Pa^{-1}$, the local heat-transfer coefficients at the feed/permeate side h_f & h_p are much higher than h_m, which is closest to the value of K_{mo}. Hence, the heat-transfer resistance of the membrane $1/h_m$ is considered to play a dominant role in determining the overall resistance $1/K_{mo}$. In this situation, the process enhancement focus should be on the membrane instead of the fluid dynamics. However, as the C value continues to increase till 1.0×10^{-6} $kg\cdot m^{-2}\cdot s^{-1}\cdot Pa^{-1}$, the curves of h_m and h_f cross each other. This indicates that the dominant effect has partially shifted from

the membrane to the feed side, so the local heat-transfer resistances from the membrane and the feed side would play equally important roles in the overall hear-transfer process. In this case, the introduction of baffles is expected to show effective enhancement on the heat/mass transfer by altering flow geometries and reducing the thermal boundary layers. The effect of membrane properties and the variation of the process enhancement strategies will be further discussed in the later sections.

Based on the above results, obviously, when the membrane dominates the heat-transfer process, any means of hydrodynamics enhancement employed on the feed side (e.g., turbulence promoters or modified fiber geometries, etc.) would show insignificant effects on improving the process performance, and the membrane should be the focus. According to equation (18), a larger *C* value and higher membrane temperature are preferable to achieve a larger h_{MD} and hence a higher permeation mass flux in MD. Different strategies are employed and compared in the following sections.

4.3 Effect of MD coefficient C on performance enhancement

4.3.1 Influential factors for the C value

Based on the most commonly reported mass-transfer mechanism, which is a combination of Knudsen and molecular diffusions through the membrane pores [2, 11], the membrane distillation coefficient *C* is a function of membrane structural parameters (i.e., pore radius, porosity, tortuosity and membrane thickness, etc.), vapor properties (i.e., molecular weight, diffusion coefficient of the solutes) as well as membrane temperature T_m. As the membrane temperature has a fairly insignificant influence on determining the *C* value [2], it can be treated as a constant for a selected membrane. In terms of structural properties, a membrane with a higher *C* value is expected to have a larger pore radius and higher porosity, smaller tortuosity and a thinner membrane wall; In other words, a higher *C* value means a reduced membrane resistance to increase h_{MD} and thus the permeability. However,

it is limited by the membrane available for MD application.

4.3.2 Effects of the C value (without/with baffles)

To explore the effect of the *C* value on MD module performance, membranes with different *C* values of 2.0×10^{-7} (the reference membrane used in the experiment, Section 3), 5.0×10^{-7} and 1.0×10^{-6} $kg\cdot m^{-2}\cdot s^{-1}\cdot Pa^{-1}$ were employed in the CFD simulations. Fig. 4 and Fig. 5 show the distributions of *TPC* and mass flux N_m curves in a single fiber module along the dimensionless fiber length *x/L*, respectively, for both non-baffled and baffled module cases.

In general, all *TPC* curves for non-baffled modules with different membranes first decrease after entering the module and then gradually increase until the exit (Fig. 4). The appearance of a characteristic U shape for *TPC* distributions along the fiber length is similar to that in our previous CFD work [17], which explained that this trend is due to the deviation of the membrane wall temperature from the fluid bulk phase at the feed and the permeate sides, i.e., the local temperature difference on the permeate side ΔT_p ($=T_{pm}-T_p$) shows an initial increase and then a subsequent decrease along its flow direction (-*x*), while on the feed side ΔT_f ($=T_f-T_{fm}$) increases continuously along the opposite direction. For modules with regularly distanced baffles, their *TPC* curves also show a slight decrease at the entrance region but generally follow an increasing trend along the fiber length. This is due to the fact that the introduction of baffles has altered the flow and promotes vortices that contribute to an enhanced mixing in the radial direction and surface renewal on the membrane surface at the feed side. In other words, the baffles have effectively prevented the build-up of hydrodynamic/thermal boundary layers near the baffle areas and hence have resulted in reduced temperature-polarization effects and increasing *TPC* distribution along the fiber length. The slight fluctuations along these curves of baffled modules are mainly due to the relatively thicker thermal boundary layers at the stagnant zones between

the membrane surface and the baffles, as shown in Fig. 6 which gives the typical temperature distributions and flow fields in non-baffled and baffled modules, respectively.

It is also noted in Fig. 4 that the *TPC* decreases significantly with increasing the *C* value from 2.0×10^{-7} to 1.0×10^{-6} kg·m^{-2}·s^{-1}·Pa^{-1}, regardless of the existence of baffles. Although a similar absolute *TPC* increment gained after incorporating baffles into the module for each type of membrane, the lowest relative percentage of improvement is from the module with the membrane of the lowest *C* value 2.0×10^{-7} kg·m^{-2}·s^{-1}·Pa^{-1} due to its reduced vulnerability to the TP effect (i.e., highest *TPC* curve).

Since *TPC* can reflect the actual driving force across the membrane, the distribution of mass flux N_m in Fig. 5 shows a similar U shape to the *TPC* curves. In general, the mass flux N_m increases dramatically with increasing *C* value due to a higher permeability of the membrane. This opposite trend (compared to the *TPC* curves) indicates that a higher mass flux tends to result in more severe temperature-polarization effect in a module. It is probably due to a more significant decrease of the surface temperature at the feed T_{fm} induced by the higher evaporation rate. Correspondingly, there is a more rapid increase of the surface temperature at the permeate T_{pm} caused by the condensation of a larger amount of vapor. Hence, a lower transmembrane temperature difference (T_{fm} - T_{pm}) is expected and thus a smaller *TPC* occurs. This explanation is consistent with the trend of the *TPC* curves in Fig. 4, in which a more permeable membrane with a higher *C* value tends to be more subjected to the TP effect. In this case, the insertion of hydrodynamic aids (e.g., baffles) in the shell-side might show significant improvement in mitigating the TP effect and enhancing the permeation flux, the relative increase of the average values can be up to from 24% to 37%, as seen in Fig. 5 when C=1.0×10^{-6} kg·m^{-2}·s^{-1}·Pa^{-1}. Whereas, for a module with relatively less permeable membranes (e.g., C=2.0×10^{-7} kg·m^{-2}·s^{-1}·Pa^{-1}), in which the heat-transfer resistance of the membrane ($1/h_m$) becomes the dominant effect, the

introduction of flow enhancing techniques such as higher circulating velocities, turbulence promoters or novel configuration designs in the shell-side flow might not have substantial influence on the overall mass- and heat-transfer processes. This conclusion is consistent with the previous discussion of Fig. 3.

4.4 Effect of membrane temperature on module performance (without/with baffles)

As mentioned previously, there are only very a few highly permeable membranes available at the laboratory scale. Therefore, for a membrane with modest permeability under specific hydrodynamic conditions, another key operating factor that can contribute to significant flux enhancement is the membrane temperature T_m.

4.4.1 Characteristic temperature

Based on the definition of h_{MD} shown in Eq. (18), the combined variable $\Delta H_{T_{fm}} \cdot \left.\frac{\mathrm{d}P}{\mathrm{d}T}\right|_{T=T_m}$ plays an equal role as the C in determining h_{MD}. Fig. 7 shows the h_{MD} as a function of membrane temperatures. It can be seen that h_{MD} increased significantly with increasing membrane temperature T_m, which suggests that choosing a higher membrane temperature is a powerful alternative to enhance the permeation flux in MD. For a different membrane with a different C value, the h_{MD} curve will show a similar trend. However, T_m only has a limited practical range determined by the feed and permeate temperatures. Also, at least 50% thermal efficiency imposes a limit to T_m. Based on the function $f(T_c)$ in Eq.(21), the characteristic membrane temperature T_c can be obtained numerically. T_c equals to 313.9K with a thermal efficiency η_h =0.5 under the experimental conditions of T_{fi}=327.2 K and T_{pi}=294 K..

Fig. 8 depicts the function $f(T_c)$ at various membrane temperatures, T_m. It shows that $f(T_c)$

increases rapidly with increasing T_m, which means that a reasonably high membrane temperature T_m is preferred for a higher thermal efficiency. It can be achieved by employing a higher feed and permeate inlet temperatures. Since T_m [given by $(T_f + T_p)/2$] is lower than the feed bulk temperature and higher than the permeate bulk temperature due to the TP effect, the operating temperature for the permeate should be slightly lower than or equal to T_c to ensure thermal efficiency η_h higher than 0.5. More discussion on the effect of operating temperatures are provided in the following sections.

4.4.2 Operating temperature

Since the vapor pressure grows exponentially with increasing temperature based on the Antoine equation, any increase of temperature will lead to a dramatic increase of vapor pressure. Also, since the vapor pressure gradient (ΔP) across the membrane is the actual driving force for MD process, a higher transmembrane temperature difference ΔT will lead to a much higher mass flux N_m. Fig. 9 shows the vapor pressure as a function of operating temperature. With the same temperature difference ΔT, the higher temperatures (both the feed and permeate) have much higher ΔP and thus larger driving force. For example, with T_p=300K, T_f=320K and *TPC* = 0.5 (at the feed side) assumed, the actual membrane surface temperature at the feed T_{fm} is 310 K, which makes the actual ΔP equal to 2739 Pa. To intensify the flows by inserting baffles or employing a higher circulating velocity, ΔP can go up to 7120 Pa for an ideal MD system with *TPC* approaching unity. However, with the same temperature difference ΔT but both temperatures increased by 10 K simultaneously, ΔP increases to 4381 Pa when *TPC*=0.5 and can further increase to the upmost of 11141 Pa when *TPC* approaches unity.

The results shown in Fig. 9 are for a series of numerical simulations conducted for non-baffled and baffled single fiber modules by simultaneously varying the feed and permeate inlet temperatures to maintain constant temperature difference ΔT, with

membrane C=2.0×10^{-7} kg·m^{-2}·s^{-1}·Pa^{-1} and constant velocities (at the feed u_{fi}=0.06 m·s^{-1} and permeate u_{pi}=0.417 m·s^{-1}). The simulation results are given in Fig. 10,11 and 12 to show the respective distributions of the *TPC*, N_m and η_h under different inlet feed/permeate temperatures along the module length L (i.e., x direction). For each set of operating temperatures (T_{fi} and T_{pi}), the temperature difference ΔT_{in} =(T_{fi} − T_{pi}) is kept constant as 33.2 K.

In Fig. 10 the *TPC* curves for both baffled and non-baffled modules have similar shapes as those shown in Fig. 4. Generally, the *TPC* decreases with increasing operating temperatures (as both feed and permeate increase simultaneously). However, the relative increase of *TPC* for the baffled modules becomes more significant with the rise of temperature when compared to non-baffled ones. Similarly, in Fig. 11(a) the N_m distributions have the same shapes as those in Fig. 5. The overall trend for N_m in both non-baffled and baffled modules is increasing with increasing operating temperatures. However, the N_m curves for baffled modules with T_{fi} ≤ 347.2 K (T_{pi} ≤ 314 K correspondingly) are below those of non-baffled modules with temperature of 13 K higher (e.g., T_{fi} =360 K & T_{pi} =326.8 K), as shown in Fig. 11 (a); This provides an evidence that raising the operating temperature would be a more effective approach to enhance the permeation flux when the membrane itself shows a dominant heat-transfer resistance (low $\Delta H_{T_{fm}} \cdot \left.\frac{\mathrm{d}P}{\mathrm{d}T}\right|_{T=T_m}$), as compared to the introduction of turbulence aids. However, the N_m curve for the baffled module at T_{fi} =360 K & T_{pi} =326.8 K exceeds that of a non-baffled configuration operated under T_{fi} =370 K & T_{pi} =333.8 K. In this case, the dominant resistance has partially shifted from the membrane to the feed flow. Therefore, the introduction of turbulence promoters or a higher circulating velocity might have a significant impact on the heat/mass transfer. To illustrate the difference for varying inlet temperatures more clearly, a comparison of local fluxes at half channel length (x=0.125m) between non-baffled and baffled modules is given in Fig. 11 (b).

In Fig. 12 the distribution of η_h increases with increasing feed temperature along the module length L (i.e., x direction), and shows that the average η_h is above 0.5 with $T_{fi} \geq$ 337.2 K and $T_{pi} \geq$ 304 K. The insertion of baffles does not show significant improvement compared to the original modules.

4.4.3 Driving force vs. temperature difference

Based on Eq. (17), to achieve a particular mass flux, the transmembrane temperature difference (T_{fm}-T_{pm}) can be reduced when h_{MD} is sufficiently large. Figs. 13 and 14 give the *TPC* and N_m distributions, respectively, for non-baffled modules at various operating temperatures and temperature differences along the module length L (i.e., x direction) when u_{fi}=0.06 m·s^{-1}, u_{pi}=0.417 m·s^{-1} and C=2.0×10^{-7} kg·m^{-2}·s^{-1}·Pa^{-1}. In Fig.13 the *TPC* distributions along the module length show a similar U shape to those shown in Fig.4. It is observed that the highest set of operating temperature T_{fi}/ T_{pi}=344 K/334 K has the lowest *TPC* curve, followed by the condition of T_{fi}/T_{pi}= 344 K/329 K; while the lowest temperature set T_{fi}/T_{pi}= 327 K/314 K shows the highest curve. This is because of a lower transmembrane temperature difference caused by a higher mass-transfer rate. Also, Fig. 13 shows that the transmembrane temperature difference (from 10 to 20K) has negligible effect on the *TPC* distributions at different inlet temperatures. In Fig.14 the mass flux N_m for the temperature set T_{fi}/ T_{pi}=344 K/334 K (ΔT_{in}=10 K) is generally higher than that of 329K/314K (ΔT_{in} =15 K), while the temperature difference of the latter is higher. Similarly, the N_m curve for a module running at T_{fi}/T_{pi}= 344 K/329 K (ΔT_{in}=15 K) is above that of the same configuration operated at 334 K/314 K which has a higher temperature difference ΔT_{in} =20 K. This is because the vapor pressure at the hot side, P_f, is the dominant factor in terms of driving force.

Fig. 15 shows the distribution of η_h along the x direction with varying operating temperatures and temperature difference under the same operating conditions as in Fig. 13.

It is found that the temperature set T_{fi}/T_{pi}=344 K/334 K has the highest thermal efficiency η_h, because it has the highest membrane temperature T_m that results in a higher h_{MD}.

The results from these two figures show that a higher operating temperature is more effective in improving permeation flux and achieving a higher thermal efficiency, even with a reasonably smaller temperature difference ΔT. Moreover, it is anticipated that a higher operating temperature on the permeate side would be more meaningful for energy recovery in a well-designed MD system, where a reasonable portion of heat from the permeate outlet could be recycled to heat the feed stream.

5. Conclusions

A series of CFD simulations were conducted for single fiber DCMD modules with and without baffles using a simplified 2D heat-transfer model in this study. The numerical simulations have been verified by experiments with less than 1% error in predicted outlet temperatures. A comprehensive analysis on the dominant effect in the MD heat-transfer process based on the resistance-in-series model was provided to reveal the impacts of key parameters that could contribute to an enhanced direct contact membrane distillation system. Potential enhancement strategies under different circumstances have been discussed.

Firstly, the effect of the *C* value on the performance of non-baffled and baffled modules was simulated. It was found that the *TPC* decreases significantly with increasing *C* value regardless of the existence of baffles; although the mass flux showed an increase trend. A membrane with a lower *C* value, which shows a dominant role in the heat-transfer process, was found to be less vulnerable to TP effects. Hence, the introduction of turbulence aids such as baffles did not show substantial process improvement in this circumstance.

However, baffles could greatly enhance the mass flux and *TPC* for a membrane with a high *C* value, where the main heat-transfer resistance is in the liquid boundary layers.

Secondly, simulations on the operating temperature for non-baffled/baffled modules with a membrane of a lower *C* value were performed. It was found that the *TPC* normally decreased with increasing operating temperatures, but showed a more significant improvement with the presence of baffles when compared to a non-baffle module at a higher temperature. Generally, the mass flux N_m increased significantly with increasing operating temperature, but to achieve a higher mass flux at relatively lower operating temperature conditions, the introduction of baffles showed less effectiveness as compared to a strategy of temperature rise. This is because the transport resistance of the membrane dominates the heat/mass transfer. However, the process improvement from hydrodynamic approaches was significant when the controlling heat-transfer resistance has partially shifted to the boundary layers under a higher operating temperature.

Finally, it was found that higher operating temperatures are preferable for substantial enhancement on the heat/mass transfer as well as MD thermal efficiency, even with a relatively smaller temperature difference. A characteristic thermal efficiency of 50%, $\eta_{h,0.5}$, can be taken as an important performance metric to evaluate the effectiveness of process enhancement approaches. Overall, this study should provide guidance to identify the dominant effects in the heat and mass transfer and identify effective strategies to improve the MD process.

Acknowledgments

Support from Siemens Water Technology is gratefully acknowledged. The authors also

thank the Singapore Economic Development Board (EDB) for funding the Singapore Membrane Technology Centre (SMTC) where this study was performed.

Nomenclature

A	membrane area (m^2)
b	membrane thickness (μm)
C	intrinsic mass-transfer coefficient of the membrane ($kg \cdot m^{-2} \cdot s^{-1} \cdot Pa^{-1}$)
c_p	specific heat capacity of material ($J \cdot kg^{-1} \cdot K^{-1}$)
h	local heat-transfer coefficient of fluids and membrane ($W \cdot m^{-2} \cdot K^{-1}$)
ΔH_T	latent heat of vaporization of water at temperature T ($J \cdot kg^{-1}$)
K	overall heat-transfer coefficient ($W \cdot m^{-2} \cdot K^{-1}$)
k	thermal conductivity ($W \cdot m^{-1} \cdot K^{-1}$)
Lx	interval between two baffles (m)
N_m	transmembrane mass flux ($kg \cdot m^{-2} \cdot s^{-1}$)
P	water vapor pressure (Pa)
Q	heat-transfer rate (W)
q	heat flux ($W \cdot m^{-2}$)
q_{MD}	transmembrane latent heat flux ($J \cdot m^{-2} \cdot s^{-1}$)
q_{HL}	conductive heat loss ($J \cdot m^{-2} \cdot s^{-1}$)
Re	Reynolds number
R_{mi}, R_{mo}	inner, outer radii of hollow fiber (m)
S	cross-sectional area of feed-side or permeate side (m^2)
S_h	source term of energy transport equation ($J \cdot m^{-3} \cdot s^{-1}$)
T	temperature (K)
v	velocity of feed or permeate ($m \cdot s^{-1}$)
u	Normalized velocity of feed or permeate ($m \cdot s^{-1}$)
x, r	axial, radial directions in cylindrical coordinate (m)

Greek letters

η_h	energy efficiency
$\bar{\bar{\tau}}$	stress tensor ($kg \cdot m^{-1} \cdot s^{-1}$)
μ	viscosity ($Pa \cdot s$)
ρ	Density ($kg \cdot m^{-3}$)
δ_r	chosen grid thickness in the *r* direction

Subscripts

b	bulk average
c	characteristic
f	feed
fm	feed-side membrane surface
m	membrane, or membrane surface
in, o	entrance, exit of the fluids
p	permeate
pm	permeate-side membrane surface

References

1. Lawson, K.W.,D.R. Lloyd, *Membrane distillation.* J. Membr. Sci., 1997. **124**(1): p. 1-25.

2. Schofield, R.W., A.G. Fane, C.J.D. Fell, *Heat and mass transfer in membrane distillation.* J. Membr. Sci., 1987. **33**(3): p. 299-313.

3. Wang, P., M.M. Teoh, T.-S. Chung, *Morphological architecture of dual-layer hollow fiber for membrane distillation with higher desalination performance.* Water Res, 45(17): p.5489-5500.

4. Song, L., B. Li, K. Sirkar, J. Gilron, *Direct contact membrane distillation-based desalination: novel membranes, devices, larger-scale studies, and a model.* Ind. Eng. Chem. Res., 2007. **46**(8): p.2307-2323.

5. Li, B.,K.K. Sirkar, *Novel Membrane and Device for Direct Contact Membrane Distillation-Based Desalination Process.* Ind. Eng. Chem. Res., 2004. **43**(17): p. 5300-5309.

6. Cath, T.Y., V.D. Adams, A.E. Childress, *Experimental study of desalination using direct contact membrane distillation: a new approach to flux enhancement.* J. Membr. Sci., 2004. **228**(1): p. 5-16.

7. Martinez, L.,J.M. Rodriquez-Maroto, *Effects of membrane and module design improvements on flux in direct contact membrane distillation.* Desalination, 2007. **205**(1-3): p. 97-103.

8. Teoh, M.M., S. Bonyadi, T.-S. Chung, *Investigation of different hollow fiber module designs for flux enhancement in the membrane distillation process.* J. Membr. Sci., 2008. **311**(1-2): p. 371-379.

9. Yang, X., R. Wang, L. Shi, A.G. Fane, M. Debowski, *Performance improvement of PVDF hollow fiber-based membrane distillation process.* J. Membr. Sci., 2011. **369**(1-2): p. 437-447.

10. Lawson, K.W.,D.R. Lloyd, *Membrane distillation. II. Direct contact MD.* J. Membr. Sci., 1996. **120**(1): p. 123-133.

11. Schofield, R.W., A.G. Fane, C.J.D. Fell, *The efficient use of energy in membrane distillation.* Desalination, 1987. **64**: p. 231-243.

12. Martinez-Diez, L.,M.I. Vazquez-Gonzalez, *A method to evaluate coefficients affecting flux in membrane distillation.* J. Membr. Sci., 2000. **173**(2): p. 225-234.

13. Qtaishat, M., T. Matsuura, B. Kruczek, M. Khayet, *Heat and mass transfer analysis in direct contact membrane distillation.* Desalination, 2008. **219**(1-3): p. 272-292.

14. El-Bourawi, M.S., Z. Ding, R. Ma, M. Khayet, *A framework for better understanding membrane distillation separation process.* J. Membr. Sci., 2006. **285**(1-2): p. 4-29.

15. Phattaranawik, J., R. Jiraratananon, A.G. Fane, C. Halim, *Mass flux enhancement using spacer filled channels in direct contact membrane distillation.* J. Membr. Sci., 2001. **187**(1-2): p. 193-201.

16. Martinez, L.,J.M. Rodriquez-Maroto, *Characterization of membrane distillation modules and analysis of mass flux enhancement by channel spacers.* J. Membr. Sci., 2006. **274**(1-2): p. 123-137.

17. Yu, H., X. Yang, R. Wang, A.G. Fane, *Numerical simulation of heat and mass transfer in direct membrane distillation in a hollow fiber module with laminar flow.* J. Membr. Sci., 2011. **384**(1-2): p. 107-116.

18. Gryta, M., M. Tomaszewska, A.W. Morawski, *Membrane distillation with laminar flow.* Sep. Purif. Technol., 1997. **11**(2): p. 93-101.

19. Gryta, M.,M. Tomaszewska, *Heat transport in the membrane distillation process.* J. Membr. Sci., 1998. **144**(1-2): p. 211-222.

20. Aravinth, S., *Prediction of heat and mass transfer for fully developed turbulent fluid flow through tubes.* Int. J. Heat Mass Transfer, 2000. **43**(8): p. 1399-1408.

21. Fimbres-Weihs, G.A.,D.E. Wiley, *Review of 3D CFD modeling of flow and mass transfer in narrow spacer-filled channels in membrane modules.* Chem. Eng. Process. **49**(7): p. 759-781.

22. Taha, T.,Z.F. Cui, *CFD modelling of gas-sparged ultrafiltration in tubular membranes.* J. Membr. Sci., 2002. **210**(1): p. 13-27.

23. Shakaib, M., S.M.F. Hasani, M. Mahmood, *CFD modeling for flow and mass transfer in spacer-obstructed membrane feed channels.* J. Membr. Sci., 2009. **326**(2): p. 270-284.

24. Zhang, L.-Z., C.-H. Liang, L.-X. Pei, *Conjugate heat and mass transfer in membrane-formed channels in all entry regions.* Int. J. Heat Mass Transfer, 2010. **53**(5-6): p. 815-824.

25. Zhang, L.-Z., *Heat and mass transfer in a quasi-counter flow membrane-based total heat exchanger.* Int. J. Heat Mass Transfer, 2010. **53**(23-24): p. 5478-5486.

26. Hwang, H.J., K. He, S. Gray, J. Zhang, I.S. Moon, *Direct contact membrane distillation (DCMD): Experimental study on the commercial PTFE membrane and modeling.* J. Membr. Sci. **371**(1-2): p. 90-98.

27. Shih, T.-H., W.W. Liou, A. Shabbir, Z. Yang, J. Zhu, *A new k-ε eddy viscosity model for high reynolds number turbulent flows.* Computers & Fluids, 1995. **24**(3): p. 227-238.

28. Thomas, L.C., *Fundamentals of heat transfer*. 1980: Prentice-Hall, Inc., Englewood Cliffs, N.J.

29. T.K. Sherwood, R.L. Pigford, C.R. Wilke, *Mass Transfer*. 1975, New York: McGraw-Hill.

30. Ding, Z., R. Ma, A.G. Fane, *A new model for mass transfer in direct contact membrane distillation.* Desalination, 2003. **151**(3): p. 217-227.

31. Bui, V.A., L.T.T. Vu, M.H. Nguyen, *Modelling the simultaneous heat and mass transfer of direct contact membrane distillation in hollow fibre modules.* J. Membr. Sci., 2010. **353**(1-2): p. 85-93.

32. Imdakm, A.O.,T. Matsuura, *Simulation of heat and mass transfer in direct contact membrane distillation (MD): The effect of membrane physical properties.* J. Membr. Sci., 2005. **262**(1-2): p. 117-128.

33. R. W. Schofield, A. G. Fane, C. J. D. Fell, R. Macoun, *Factors affecting flux in membrane distillation.* Desalination, 1990. **77**: p. 279-294.

34. Rohsenow, W.M.,J.P. Hartnett, *Handbook of heat transfer*. 1973: McGraw-Hill, Inc.

List of Figures

Fig. 10. *TPC* distribution along the module length for non-baffled and baffled modules at varied feed/permeate inlet temperatures with a constant temperature difference (ΔT_{in}=33.2 K, u_{fi}=0.06 m·s^{-1}, u_{pi}=0.417 m·s^{-1}, C = 2.0×10^{-7} kg·m^{-2}·s^{-1}·Pa^{-1})

Fig. 11. N_m distribution along the module length for non-baffled and baffled modules at ΔT_{in} (a) N_m distribution along the module length; (b) local mass fluxes N_m comparison x=0.125m (ΔT_{in}=33.2 K, u_{fi}=0.06 m·s^{-1}, u_{pi}=0.417 m·s^{-1}, C = 2.0×10^{-7} kg·m^{-2}·s^{-1}·Pa^{-1})

Fig. 12. η_h distribution along the module length for non-baffled and baffled modules at varied feed/permeate inlet temperatures with a constant temperature difference (ΔT_{in}=33.2 K, u_{fi}=0.06 m·s^{-1}, u_{pi}=0.417 m·s^{-1}, C = 2.0×10^{-7} kg·m^{-2}·s^{-1}·Pa^{-1})

Fig. 13. *TPC* distributions along the module length at varied feed/permeate inlet temperatures T_{fi}/T_{pi} and temperature differences ΔT_{in} (u_{fi}=0.06 m·s^{-1}, u_{pi}=0.417 m·s^{-1}, C = 2.0×10^{-7} kg·m^{-2}·s^{-1}·Pa^{-1})

Fig. 14. N_m distributions along the module length at varied feed/permeate inlet temperatures T_{fi}/T_{pi} and temperature differences ΔT_{in} (u_{fi}=0.06 m·s^{-1}, u_{pi}=0.417 m·s^{-1}, C = 2.0×10^{-7} kg·m^{-2}·s^{-1}·Pa^{-1})

Fig. 15. η_h distributions along the module length at varied feed/permeate inlet temperatures T_{fi}/T_{pi} and temperature differences ΔT_{in} (u_{fi}=0.06 m·s^{-1}, u_{pi}=0.417 m·s^{-1}, C = 2.0×10^{-7} kg·m^{-2}·s^{-1}·Pa^{-1})

List of Tables

Table 1. The temperature comparison of experimental data and simulation results (u_{fi}=0.06 m·s^{-1}, u_{pi}=0.417 m·s^{-1}, C = 2.0×10^{-7} kg·m^{-2}·s^{-1}·Pa^{-1})

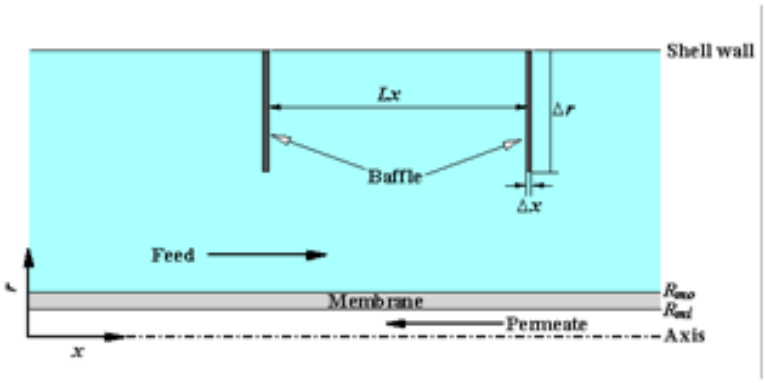

Fig. 1. Schematic of axially-symmetry single fiber module in CFD simulating domain

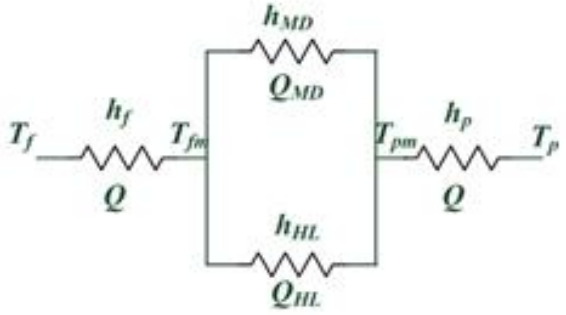

Fig. 2. Schematic of heat transfer process in MD

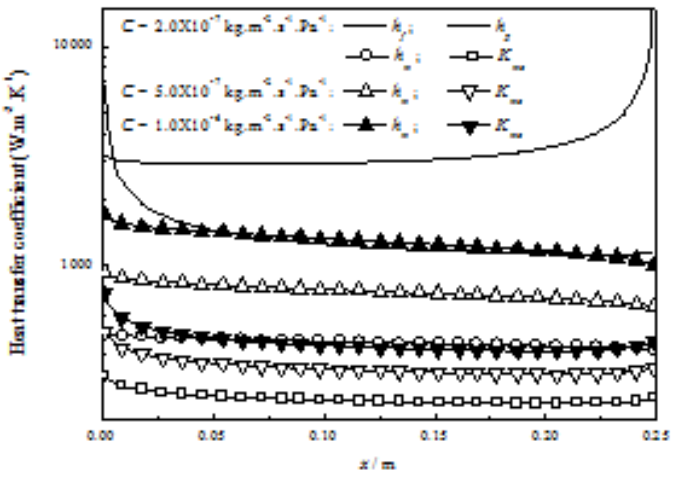

Fig. 3. Heat-transfer coefficient distributions along the module length for membranes with different C values (T_{f0} = 327.2 K, T_{p0} = 294.0 K, u_{f0}=0.06 m·s^{-1}, u_{p0}= 0.417 m·s^{-1}, $C = 2.0\times10^{-7}$ to 1.0×10^{-6} kg·m^{-2}·s^{-1}·Pa^{-1})

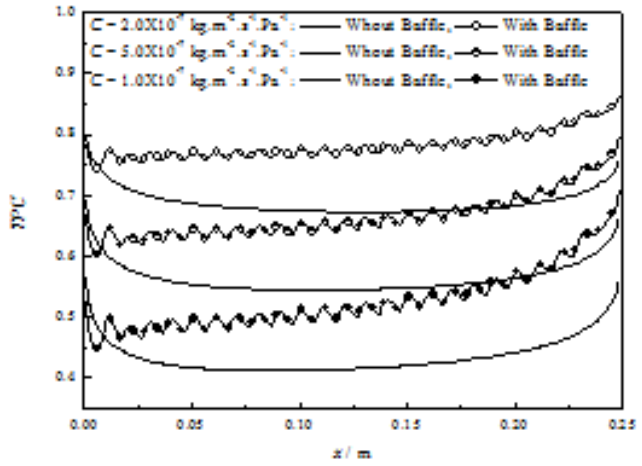

Fig. 4. *TPC* distributions along the module length for non-baffled and baffled modules with membranes of different C values (T_{f0} = 327.2 K, T_{p0} = 294.0 K, u_{f0}=0.06 m·s^{-1}, u_{p0}= 0.417 m·s^{-1}, $C = 2.0\times10^{-7}$ to 1.0×10^{-6} kg·m^{-2}·s^{-1}·Pa^{-1})

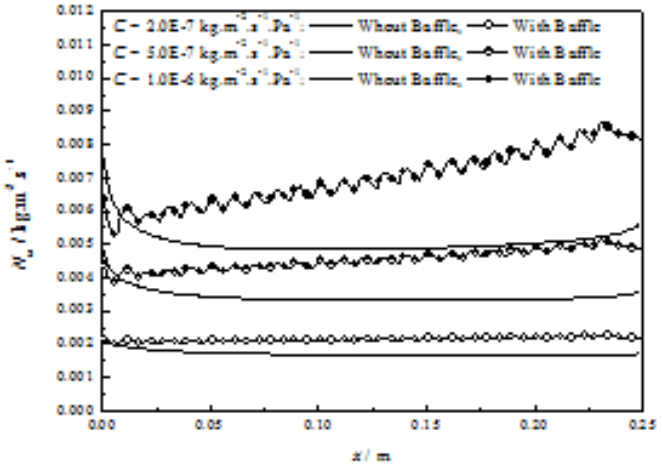

Fig. 5. N_w distributions along the module length for non-baffled and baffled modules with membranes of different C values
(T_{f0} = 327.2 K, T_{p1} = 294.0 K, u_{f0}=0.06 m·s^{-1}, u_{p1}= 0.417 m·s^{-1}, C = 2.0 × 10^{-7} to 1.0 × 10^{-6} kg·m^{-2}·s^{-1}·Pa^{-1})

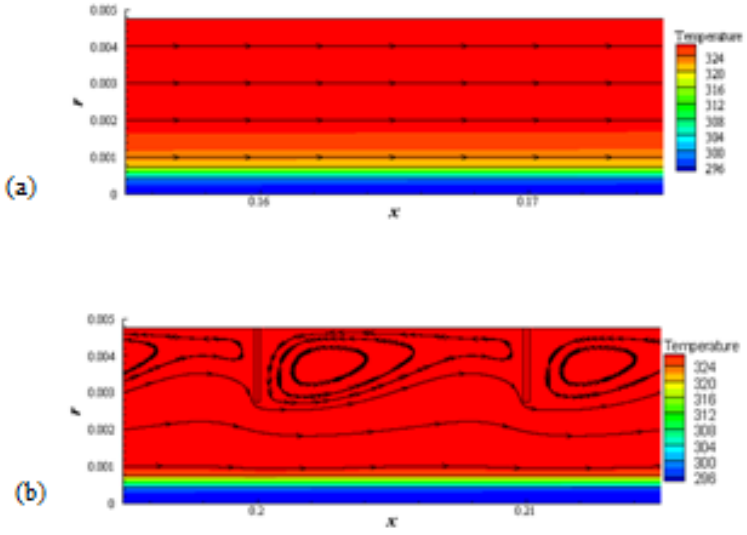

Fig. 6. Temperature distributions and flow fields at the shell side of 0.25m modules (local snapshots)
(a) without baffles; (b) with baffles
(T_{f0} = 327.2 K, T_{p1} = 294.0 K, u_{f0}=0.06 m·s^{-1}, u_{p1}= 0.417 m·s^{-1}, C = 2.0 × 10^{-7} kg·m^{-2}·s^{-1}·Pa^{-1})

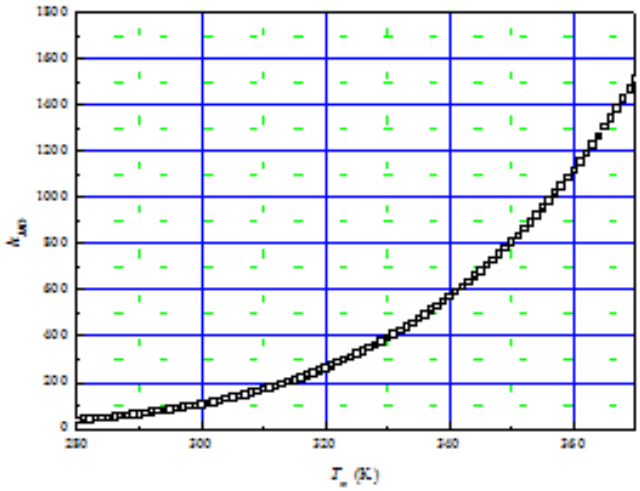

Fig. 7. h_{MD} vs. membrane temperature T_m with $C = 2.0 \times 10^{-7}$ kg·m^{-2}·s^{-1}·Pa^{-1}

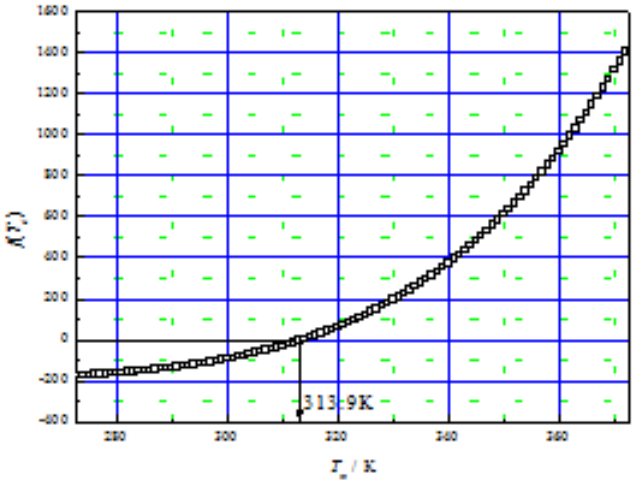

Fig. 8. Function $f(T_c)$ at varied membrane temperatures T_m with $C = 2.0 \times 10^{-7}$ kg·m^{-2}·s^{-1}·Pa^{-1}

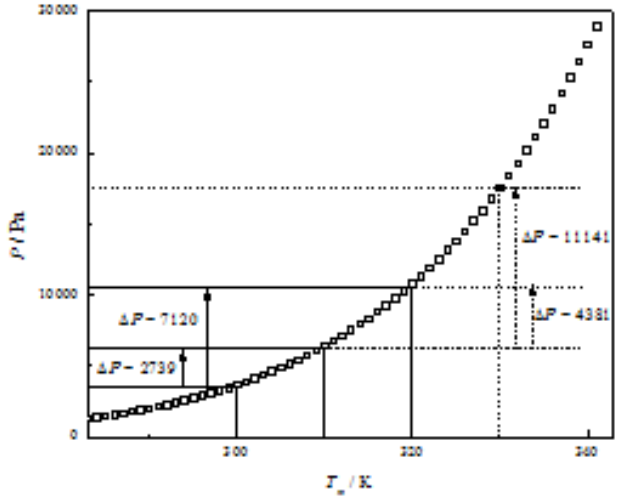

Fig. 9. The distribution of saturated vapor pressure difference ΔP at various membrane temperatures T_m

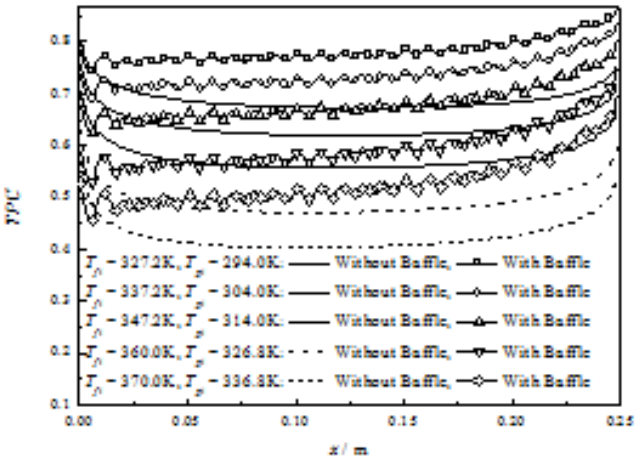

Fig. 10. *TPC* distribution along the module length for non-baffled and baffled modules at varied feed/permeate inlet temperatures with a constant temperature difference (ΔT_{in}=33.2 K, u_{fi}=0.06 m·s^{-1}, u_{pi}= 0.417 m·s^{-1}, $C = 2.0 \times 10^{-7}$ kg·m^{-2}·s^{-1}·Pa^{-1})

(a) N_m distribution along the module length

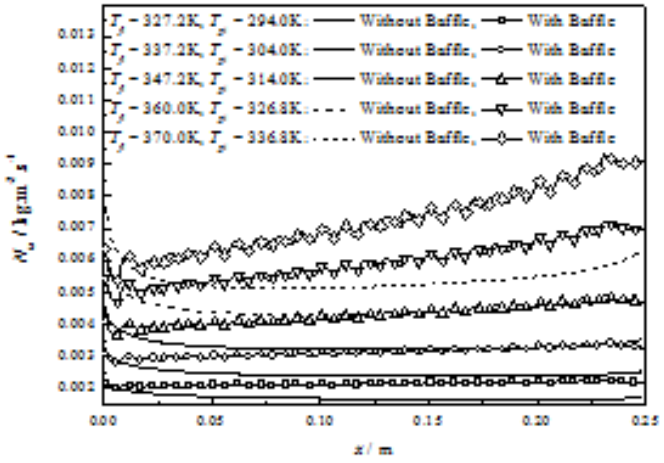

(b) Local mass fluxes N_m comparison (x=0.125m)

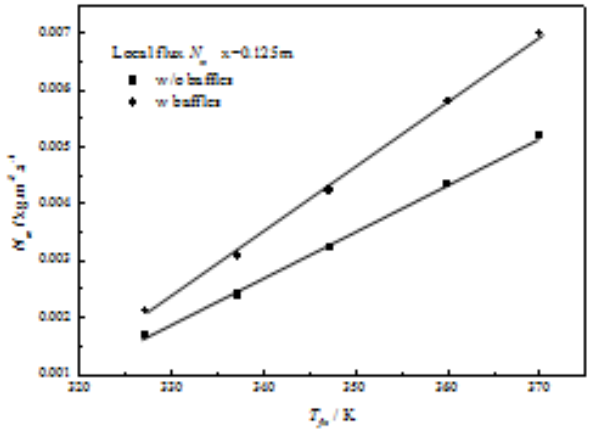

Fig. 11. N_m results for non-baffled and baffled modules at varied feed/permeate inlet temperatures with a constant temperature difference ΔT_{in} (a) N_m distribution along the module length; (b) Local mass fluxes N_m comparison x=0.125m (ΔT_{in}=33.2 K, u_{f1}=0.0602 m·s^{-1}, u_{p1}= 0.417 m·s^{-1}, $C = 2.0 \times 10^{-7}$ kg·m^{-2}·s^{-1}·Pa^{-1})

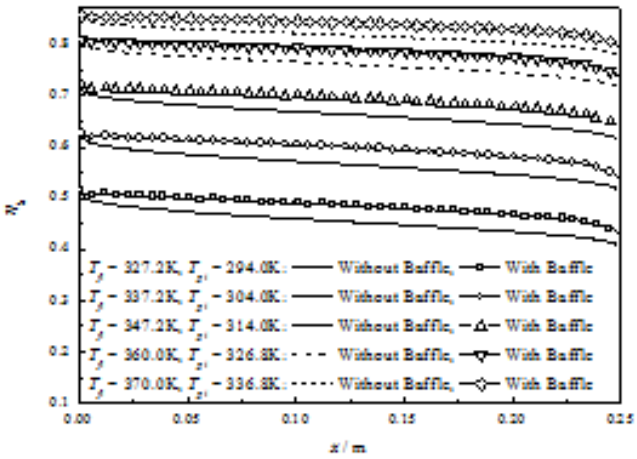

Fig. 12. η_k distribution along the module length for non-baffled and baffled modules at varied feed/permeate inlet temperatures with a constant temperature difference (ΔT_{in}=33.2 K, u_{f0}=0.06 m·s^{-1}, u_{p0}= 0.417 m·s^{-1}, C = 2.0 × 10^{-7} kg·m^{-2}·s^{-1}·Pa^{-1})

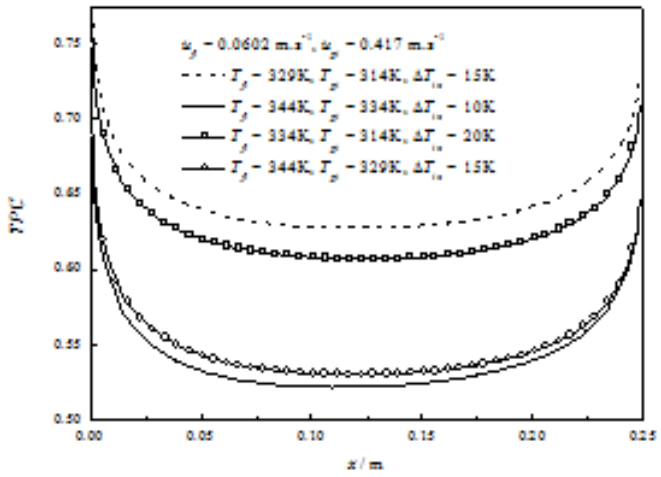

Fig. 13. TPC distributions along the module length at varied feed/permeate inlet temperatures T_{f0}/ T_{p1} and temperature differences ΔT_{in} (u_{f0}=0.06 m·s^{-1}, u_{p1}= 0.417 m·s^{-1}, C = 2.0 × 10^{-7} kg·m^{-2}·s^{-1}·Pa^{-1})

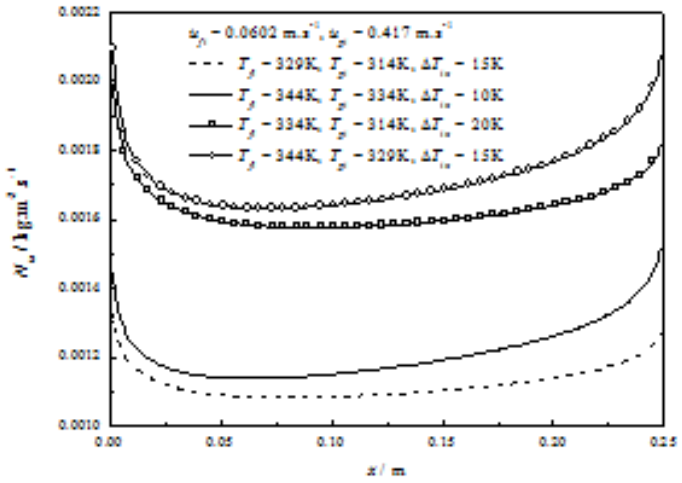

Fig. 14. N_m distributions along the module length at varied feed/permeate inlet temperatures T_{f1}/ T_{p1} and temperature differences ΔT_{in}
(u_{f1}=0.06 m·s^{-1}, u_{p1}= 0.417 m·s^{-1}, $C = 2.0 \times 10^{-7}$ kg·m^{-2}·s^{-1}·Pa^{-1})

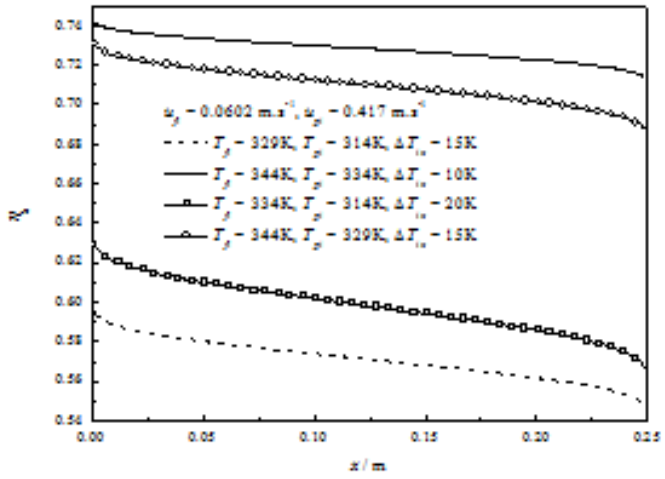

Fig. 15. η_h distributions along the module length at varied feed/permeate inlet temperatures T_{f1}/ T_{p1} and temperature differences ΔT_{in}
(u_{f1}=0.06 m·s^{-1}, u_{p1}= 0.417 m·s^{-1}, $C = 2.0 \times 10^{-7}$ kg·m^{-2}·s^{-1}·Pa^{-1})

Table. 1. The temperature comparison of experimental data and simulation results
(u_{fi}=0.06 m·s^{-1}, u_{pi}= 0.417 m·s^{-1}, $C = 2.0 \times 10^{-7}$ kg·m^{2}·s^{-1}·Pr^{-1})

L (m)		T_{fi} (K)	T_{fo} (K)	Error (%)	T_{pi} (K)	T_{po} (K)	Error (%)
0.25	Exp.	327.2	325.7	-	294.0	301.4	-
	Sim.	-	325.9	0.0614		300.9	-0.166
0.25	Exp.	333.9	331.6	-	294.4	302.8	-
	Sim.		332.5	-0.271		303.2	0.132
0.25	Exp.	334.8	333.8	-	312.8	317.7	-
	Sim.	-	333.6	-0.0599		318.3	0.189
0.25	Exp.	337.6	334.8	-	294.3	304.1	-
	Sim.		336.2	0.418		304.2	0.0329
0.25	Exp.	337.6	336.4	-	304.0	311.1	-
	Sim.		336.3	-0.0297		312.1	0.321